Petroleum Science 23 (2026) 2545–2559

Contents lists available at ScienceDirect

Petroleum Science

journal homepage: www.keaipublishing.com/en/journals/petroleum-science

Original Paper

Coordinate-transformation-based fast sweeping method for the factored eikonal equation on triangular meshes

Xin Chen [a,b], Dan-Ping Cao [a,b], Zhao-Lin Zhu [c], Xin Fu [a,b,*]

[a] School of Geosciences, China University of Petroleum (East China), Qingdao, 266580, Shandong, China
[b] State Key Laboratory of Deep Oil and Gas, China University of Petroleum (East China), Qingdao, 266580, Shandong, China
[c] Hainan Institute of Zhejiang University, Sanya, 572024, Hainan, China

ARTICLE INFO

Article history:
Received 15 June 2025
Received in revised form
23 November 2025
Accepted 20 January 2026
Available online 23 January 2026

Edited by Meng-Jiao Zhou

Keywords:
Traveltime
Fast sweeping method
Unstructured triangular mesh
Factored eikonal equation

ABSTRACT

Accurate traveltime computation in complex geometries is crucial for seismological applications such as traveltime tomography and migration. However, eikonal solvers relying on finite-differences encounter the source singularity, leading to numerical errors that propagate throughout the computational domain and compromise traveltime accuracy. Solving the factored eikonal equation has proven effective in addressing this singularity, but it has not yet been applied to triangular meshes, which are significant for modeling complex geological structures and irregular topographies. To address this challenge, we propose a new coordinate-transformation-based fast sweeping method (FSMCT) designed for triangular meshes. FSMCT maps each triangular element in the physical domain into a canonical reference triangle through coordinate transformation, and constructs an upwind finite-difference scheme on the reference triangle to solve the eikonal equation. The framework enables a straight forward extension to the multiplicatively/additively factored eikonal equations, overcoming the long-standing limitation that the conventional fast sweeping method (FSM) cannot solve the factored eikonal equation on triangular meshes, thereby effectively mitigating source singularity. Furthermore, FSMCT solves the eikonal equation on the reference triangle, while existing FSM typically require further subdivision of obtuse triangles. Numerical simulations demonstrate that FSMCT accurately solves the factored eikonal equation on triangular meshes, substantially reducing the errors caused by source singularity and achieving significantly higher accuracy than the conventional FSM.

1. Introduction

Traveltime is crucial in various areas of seismology, including pre-stack migration (Cheng et al., 2016; Li et al., 2009; Xin et al., 2018), traveltime tomography (Huang and Bellefleur, 2012; Li et al., 2023; Wang et al., 2022; Zhao et al., 2019), slope tomography (Sambolian et al., 2019; Tavakoli et al., 2017), and earthquake location (Zhang et al., 2023b). Its forward modeling serves as the foundation for inversion, and its computational accuracy directly impacts the quality of the inversion results. In seismic exploration, traveltime calculations primarily rely on ray tracing methods (Bai et al., 2010; Xu et al., 2006; Zhao et al., 1992) and eikonal equation solvers (Hassouna and Farag, 2007; Vidale, 1988, 1990).

Eikonal equation solvers offer higher computational efficiency and can provide accurate seismic traveltimes in complex models. Within the framework of high-frequency approximation, eikonal equation solvers are one of the main approaches for traveltime computation, offering high computational efficiency and the ability to provide widely covered seismic traveltime fields in complex models. Vidale (1988) first proposed using the finite-difference (FD) scheme on rectangular meshes to solve the eikonal equation, and since then, eikonal solvers have undergone significant development (Rawlinson and Sambridge, 2004; Sethian, 1999; Sethian and Popovici, 1999). One of the most notable advancements is the fast sweeping method (FSM) (Zhao, 2004), which utilizes Gauss-Seidel iteration to sweep the computational domain and is a simple yet efficient approach to solving the eikonal equation.

* Corresponding author.
E-mail address: xin.fu1@outlook.com (X. Fu).
Peer review under the responsibility of China University of Petroleum (Beijing).

https://doi.org/10.1016/j.petsci.2026.01.032

When dealing with point source conditions, finite-difference (FD) based eikonal solvers inevitably encounter errors caused by source singularity (Luo and Qian, 2012; Treister and Haber, 2016; Zhou et al., 2020). The errors propagate from the source to the entire computational domain, negatively impacting the accuracy of traveltime calculations. To address this challenge, local grid refinement techniques have been suggested as a solution, where the grid near the source is refined to suppress singularity-induced errors (Rawlinson and Sambridge, 2004; Zhang et al., 2021). However, this approach also has its limitations. It increases computational complexity and reduces the overall efficiency of traveltime calculations (Rawlinson et al., 2006; Zhou et al., 2020).

Fomel et al. (2009) first introduced the multiplicative factorization approach to enhance the accuracy of the fast sweeping method (FSM) in traveltime calculations. This approach decomposes the unknown traveltime function into two factors: the first factor, which captures the source singularity analytically, and the second, a corrective term obtained by solving the factored eikonal equation. Due to its effectiveness, this factorization method has been widely adopted. Tavakoli et al. (2015) further utilized the factored approach to solve the eikonal equation in TTI media, eliminating initial errors through factorization. Huang and Luo (2020) presented hybrid fast-sweeping methods for calculating first-arrival traveltime by solving the factored anisotropic eikonal equation. Qiao et al. (2024) proposed the adaptive finite-difference (AFD) method to obtain high-precision 3D seismic traveltimes, in which the multiplicative factor decomposition method is adopted to reduce errors caused by the source singularity. However, existing factored eikonal solvers are primarily implemented on rectangular meshes, which limits their applicability to complex geometric cases. In real-world applications, work areas often feature irregular topographies and subsurface interfaces, such as mountainous structures, crustal boundaries, and the Moho discontinuity (Zhang et al., 2021, 2023a). Unstructured triangular meshes offer greater adaptability, making them advantageous for calculating traveltime in complex models. Compared with rectangular meshes, triangular meshing is more flexible. In the presence of irregular subsurface interfaces and complex structures, triangular meshes can be locally refined in an adaptive manner to better represent the complex underground structural features (Jacquet, 2021; Qiu et al., 2020; Schall et al., 2004).

In this study, we employ unstructured triangular meshes for traveltime computation in complex geometries. Early studies explored solving the eikonal equation on triangular meshes (Barth and Sethian, 1998; Kimmel and Sethian, 1998). Since Qian et al. (2007) extended FSM to unstructured triangular meshes for solving the eikonal equation, triangular-mesh-based FSM has seen rapid development and achieved notable progress (Zhang et al., 2021, 2023a, 2023b). Similar to rectangular-mesh-based FSM, triangular-mesh-based FSM also exhibits source singularity, as illustrated in Fig. 1. At present, the application of the factorization approach in triangular-mesh-based FSM remains largely unexplored, highlighting the need to develop new algorithms to improve traveltime accuracy in geometrically complex models.

To achieve high-precision seismic traveltimes in complex geometries, we propose a coordinate-transformation-based fast sweeping method (FSMCT) on triangular meshes to solve the factored eikonal equation, overcoming source singularity and improving the accuracy of traveltime calculation. Coordinate transformation, a method commonly used in discontinuous Galerkin methods for solving wave equations (Cordier et al., 2005; He and Yue, 2019; Käser and Dumbser, 2006; Qiu et al., 2020), is introduced here for the eikonal equation. By applying this transformation, we transform any physical triangle in the Cartesian coordinate system into a canonical reference triangle in a reference coordinate system. On the normalized reference triangle, we discretize the eikonal equation using the causality-preserving upwind finite-difference (FD) scheme (Fomel et al., 2009; Huang et al., 2019), ensuring stable traveltime propagation. By extending FSMCT to solve eikonal equations with multiplicative factorization (FSMCTM) and additive factorization (FSMCTA), it effectively suppresses source singularity on triangular meshes. Additionally, when unstructured triangular meshes are used to model irregular geological interfaces, obtuse triangles are inevitable. Traditional FSMs may encounter accuracy issues or even errors when directly solving the eikonal equation on obtuse physical triangles (Fu et al., 2011; Qian et al., 2007). The conventional approach involves splitting obtuse triangles by connecting the vertex with the vertex of the neighboring triangle, but the irregular arrangement of unstructured triangular meshes renders such post-processing operations cumbersome and error-prone. In contrast, FSMCT avoids subdivision of obtuse triangles because all discretization operations are performed on the canonical reference triangle. Numerical tests in various models demonstrate that triangular-mesh-based FSMCT enables accurate and efficient calculation of traveltime, even for complex models with rugged topographies and irregular subsurface interfaces.

In this paper, we first introduce the FSMCT for solving the eikonal equation on triangular meshes. Then, we describe its extension to the factored eikonal equation in detail. Afterward, we demonstrate the accuracy of the algorithm through several numerical examples. Finally, we discuss its advantages, outline potential future extensions, and draw several conclusions.

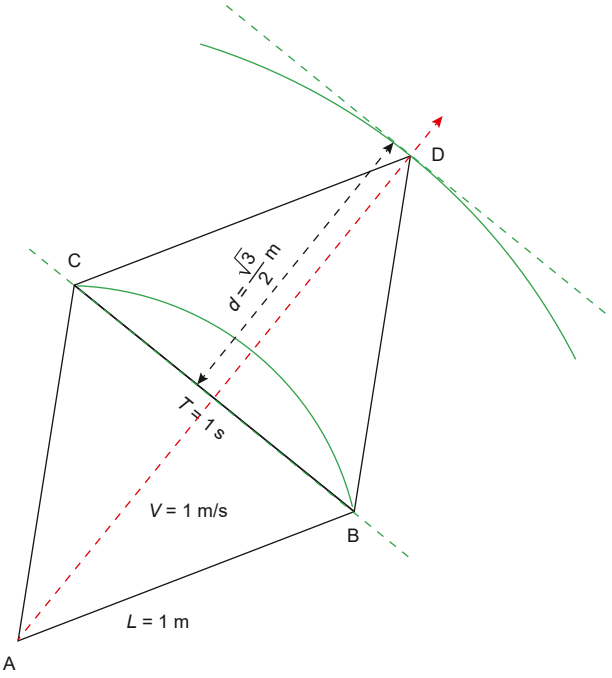

Fig. 1. Illustration of the computation error caused by the point source singularity. The red dashed line is the characteristic line, which is the propagation direction of the seismic wave. The side length is 1 m in the equilateral triangular meshes, and the seismic velocity is 1 m/s. The traveltime T_A of source point is set to 0 s, the traveltime T_B and T_C can be accurately calculated as 1 s. The eikonal solver approximates the wavefront using the plane wave (the green dashed line), and the traveltime T_D can be calculated as $(1+\frac{\sqrt{3}}{2})$ s. However, the analytical solution of the point D is $\sqrt{3}$ s.

2. Method

2.1. FSMCT for the eikonal equation

2.1.1. Local solver for the eikonal equation

In isotropic media, the eikonal equation is typically expressed as:

$$\left(\frac{\partial T}{\partial x}\right)^2+\left(\frac{\partial T}{\partial z}\right)^2=S^2, \tag{1}$$

where $T(x,z)$ denotes the traveltime from source to the point (x,z), and $S(x,z)$ is the slowness depending on the position (x,z).

When solving the 2D eikonal equation for an isotropic model, we employ unstructured triangular meshes to partition the model. For a given physical triangle ΔABC, given the traveltime T_A and T_B at points A and B, we aim to estimate the traveltime T_C at point C. To make the eikonal equation solver suitable for any angled triangular mesh, we transform each physical triangle *Tri* to a reference triangle Tri_E in the uv-reference coordinate system, as shown in Fig. 2. And then we can solve the eikonal equation on the reference triangle Tri_E.

It is worth noting that the traveltime T and slowness S at the corresponding points on the physical triangle *Tri* and the reference triangle Tri_E are equal. The coordinate transformation is defined by:

$$\begin{aligned} x&=x_C+(x_A-x_C)u+(x_B-x_C)v,\\ z&=z_C+(z_A-z_C)u+(z_B-z_C)v. \end{aligned} \tag{2}$$

The corresponding inverse transformation is given by:

$$\begin{aligned} u&=\frac{1}{|\mathbf{J}|}((x_Bz_C-x_Cz_B)+x(z_B-z_C)+z(x_C-x_B)),\\ v&=\frac{1}{|\mathbf{J}|}((x_Cz_A-x_Az_C)+x(z_C-z_A)+z(x_A-x_C)), \end{aligned} \tag{3}$$

where $|\mathbf{J}|=(x_A-x_C)(z_B-z_C)-(x_B-x_C)(z_A-z_C)$ is the determinant of the Jacobian matrix of the transformation. Furthermore, by taking the first-order derivative of Eq. (3), we obtain:

$$\begin{aligned} \frac{\partial u}{\partial x}&=\frac{z_B-z_C}{|\mathbf{J}|}=J_{11},\frac{\partial u}{\partial z}=\frac{x_C-x_B}{|\mathbf{J}|}=J_{12},\\ \frac{\partial v}{\partial x}&=\frac{z_C-z_A}{|\mathbf{J}|}=J_{21},\frac{\partial v}{\partial z}=\frac{x_A-x_C}{|\mathbf{J}|}=J_{22}. \end{aligned} \tag{4}$$

According to the chain rule, the differential terms in the eikonal equation can be rewritten as:

$$\begin{aligned} \frac{\partial T}{\partial x}&=\frac{\partial T}{\partial u}\frac{\partial u}{\partial x}+\frac{\partial T}{\partial v}\frac{\partial v}{\partial x},\\ \frac{\partial T}{\partial z}&=\frac{\partial T}{\partial u}\frac{\partial u}{\partial z}+\frac{\partial T}{\partial v}\frac{\partial v}{\partial z}. \end{aligned} \tag{5}$$

Using the above equations, we have completed the coordinate transformation of the triangular, allowing us to discretize the differential term of eikonal equation in the uv-reference system. On the reference triangle Tri_E, we use first-order difference to approximate the partial derivatives of T:

$$\frac{\partial T}{\partial u}=\frac{T_A-T_C}{\Delta u},\frac{\partial T}{\partial v}=\frac{T_B-T_C}{\Delta v}. \tag{6}$$

By putting the above equations into Eq. (5), we have:

$$\begin{aligned} \frac{\partial T}{\partial x}&=\frac{T_A-T_C}{\Delta u}J_{11}+\frac{T_B-T_C}{\Delta v}J_{21},\\ \frac{\partial T}{\partial z}&=\frac{T_A-T_C}{\Delta u}J_{12}+\frac{T_B-T_C}{\Delta v}J_{22}. \end{aligned} \tag{7}$$

Then, Eq. (1) can be discretized as:

$$\left(\frac{T_A-T_C}{\Delta u}J_{11}+\frac{T_B-T_C}{\Delta v}J_{21}\right)^2+\left(\frac{T_A-T_C}{\Delta u}J_{12}+\frac{T_B-T_C}{\Delta v}J_{22}\right)^2=S^2. \tag{8}$$

The above equation is a quadratic equation with an unknown variable T_C and gives the following solution:

$$T_C=\frac{-b\pm\sqrt{b^2-4ac}}{2a}, \tag{9}$$

where

$$\begin{aligned} a&=J_{11}^2+J_{12}^2+J_{21}^2+J_{22}^2+2J_{11}J_{21}+2J_{12}J_{22},\\ b&=-2T_A\left(J_{11}^2+J_{12}^2\right)-2T_B\left(J_{21}^2+J_{22}^2\right)-2(T_A+T_B)(J_{11}J_{21}+J_{12}J_{22}),\\ c&=T_A^2\left(J_{11}^2+J_{12}^2\right)+T_B^2\left(J_{21}^2+J_{22}^2\right)+2T_AT_B(J_{11}J_{21}+J_{12}J_{22})-S^2. \end{aligned} \tag{10}$$

There are two scenarios to consider when solving Eq. (8). Firstly, there is no solution for T_C, we can compute it by $T_C=\min(T_A+L_{AC}\cdot S, T_B+L_{BC}\cdot S)$, where L_{AC} and L_{BC} denote the lengths of edges AC and BC, respectively.

However, when Eq. (8) does have solutions (either one or two), we must deliberate on whether to accept those solutions.

Assuming the traveltime at node c is determined within the triangle depicted in Fig. 3, we denote $\angle BAC=\alpha$ and $\angle ABC=\beta$; L_{AB},

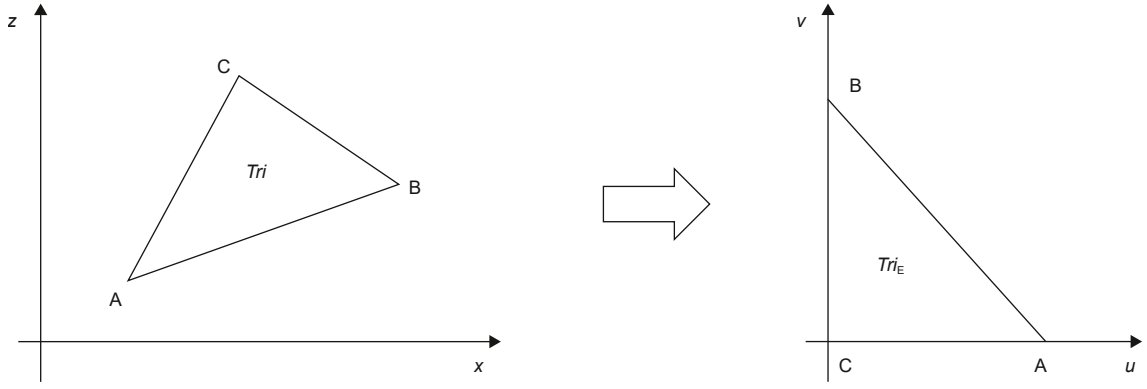

Fig. 2. Illustration of the coordinate transformation from the physical triangle *Tri* to the reference triangle Tri_E with nodes at (0, 0), (0, 1), and (1, 0).

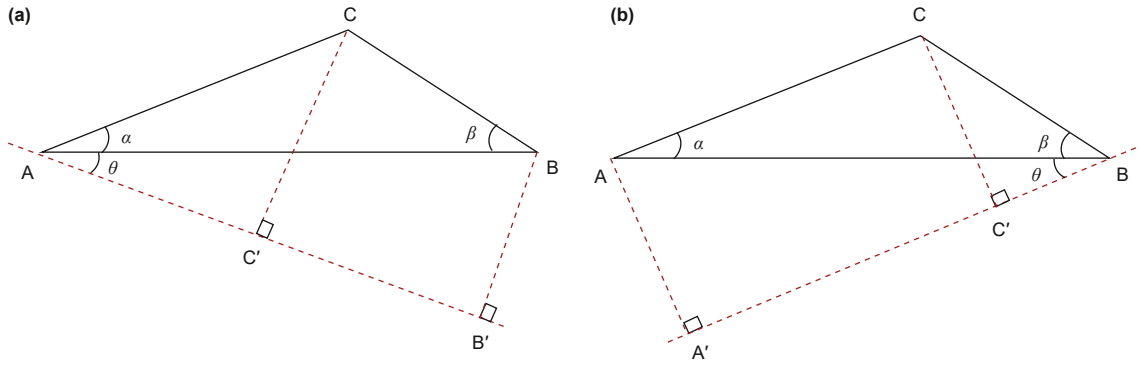

Fig. 3. Illustration of updating the value at node C in a triangle when the specified condition is satisfied. **(a)** The wavefront passes through A first rather than B. **(b)** The wavefront passes through B first rather than A.

L_{BC} and L_{AC} are the lengths of the edges AB, BC, and AC, respectively. Our initial step is to ascertain whether the wavefront passes through node A or node B first. If the wavefront AC′ reaches A first (Fig. 3(a)), and the calculated T_C must fulfill the following conditions:

(1) Angle condition: Using the given formula: $\theta = \arcsin\frac{T_{BB'}}{L_{AB}\cdot S}$, where $T_{BB'} = T_B - T_A$, we can derive that when $\theta = 0°$, the wavefront is perpendicular to the edge AB, and when $\theta + \alpha = 90°$, the wavefront is perpendicular to the edge AC. Therefore, to ensure that the perpendicular line falls within the triangle, the angle condition should meet the condition $\theta \geq 0°$ and $\theta + \alpha \leq 90°$.
(2) Numerical condition: Because the wavefront arrives at A before reaching the node C, we use the traveltime T_A to determine whether the obtained T_C is acceptable. The numerical condition requires that $T_C > T_A$ and $T_C > T_B$.

In summary, the key conditions are $\theta \geq 0°$, $\theta + \alpha \leq 90°$, $T_C > T_A$ and $T_C > T_B$. If the wavefront traverses B first instead of A (Fig. 3(b)), the conditions remain analogous.

When determining the traveltime at node D, it's crucial to consider its surrounding triangles (Fig. 4). Solve Eq. (8) on the surrounding triangles to obtain the numerical solutions, and then choose the minimum value as the traveltime for the current node D.

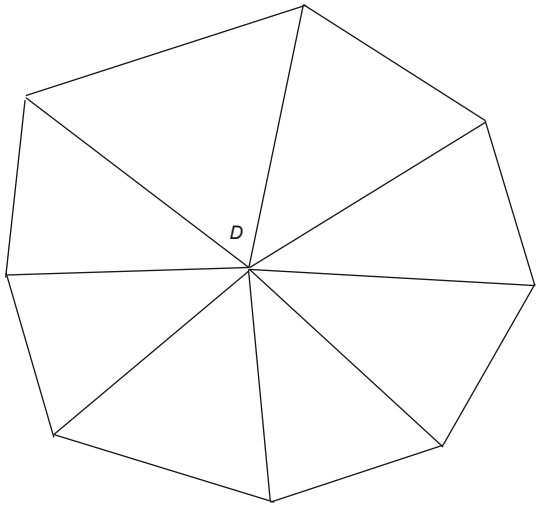

Fig. 4. Illustration of node D and its associated triangles in a triangular mesh.

2.1.2. Algorithm 1: FSMCT for eikonal equation

After discussing the local solver for the eikonal equation in the previous section, let us outline the full FSMCT algorithm as follows:

1. Initialization.

Divide the computational domain into triangles and assign labels to all the nodes. For the node where the source is positioned, set the traveltime T to 0. For all other nodes, initialize the traveltimes with a large positive number, which will be updated during the subsequent iterations.

2. Preprocessing.

We utilize the ordering method suggested by Qian et al. (2007), which involves selecting three corner points as reference points. We then arrange all nodes in ascending and descending order based on their L_2-distance from the reference point. This strategy guarantees that the Gauss-Seidel iterations within the FSM capture the characteristics of all directions. Subsequently, we store the indices of the sorted nodes in arrays:

$$\begin{aligned} &S_R^+ : \text{ascentorder}, R = 1,2,3; \\ &S_R^- : \text{descentorder}, R = 1,2,3. \end{aligned} \tag{11}$$

3. Gauss-Seidel iteration.
   (1) For $R = 1,2,3$:
   (2) For $S = +-$:

We use the local solver to obtain the traveltime T_n of n triangles around the current node, $n = 1,2,3,\cdots$. Then select the minimum value as the traveltime T for the current node.

4. Stopping rule.

If the convergence criterion $|t_n - t_{n-1}| < \epsilon$ is satisfied, in which ϵ is a very small positive number, the iteration stops.

2.2. FSMCT for the factored eikonal equation

2.2.1. Local solver for the factored eikonal equation: multiplicatively and additively

To mitigate the adverse effects of the point source singularity on accuracy, we employ a factorization approach to the solution of the eikonal equation, utilizing both multiplicative and additive

factors. Traveltime T can be decomposed into two multiplicative factors:

$$T = T_0 \tau, \tag{12}$$

or two additive factors:

$$T = T_0 + \tau, \tag{13}$$

where T_0 can capture the source singularity, which can be calculated through $\left(\frac{\partial T_0}{\partial x}\right)^2 + \left(\frac{\partial T_0}{\partial z}\right)^2 = S_O^2$ (S_O is the slowness at the source). The τ is the unknown factor that is smooth near the source. Using two factors to recover T, the accuracy of solving T has been improved compared to directly solving Eq. (1).

Putting Eq. (12) into Eq. (1), we can obtain the multiplicatively factored eikonal equation:

$$\left(\frac{\partial T_0}{\partial x}\tau + T_0\frac{\partial \tau}{\partial x}\right)^2 + \left(\frac{\partial T_0}{\partial z}\tau + T_0\frac{\partial \tau}{\partial z}\right)^2 = S^2, \tag{14}$$

and putting Eq. (13) into Eq. (1), the additively factored eikonal equation is:

$$\left(\frac{\partial T_0}{\partial x} + \frac{\partial \tau}{\partial x}\right)^2 + \left(\frac{\partial T_0}{\partial z} + \frac{\partial \tau}{\partial z}\right)^2 = S^2, \tag{15}$$

$\frac{\partial T_0}{\partial x}$ and $\frac{\partial T_0}{\partial z}$ in Eqs. (14) and (15) can be calculated using the following equation:

$$\begin{aligned}
\frac{\partial T_0}{\partial x} &= T_{0x} = \frac{x - x_O}{\sqrt{(x - x_O)^2 + (z - z_O)^2}} S_O, \\
\frac{\partial T_0}{\partial z} &= T_{0z} = \frac{z - z_O}{\sqrt{(x - x_O)^2 + (z - z_O)^2}} S_O.
\end{aligned} \tag{16}$$

Coordinate transformation adopted by the FSMCT can be naturally extended to compute $\frac{\partial \tau}{\partial x}$ and $\frac{\partial \tau}{\partial z}$, which can be expressed as:

$$\begin{aligned}
\frac{\partial \tau}{\partial x} &= \frac{\partial \tau}{\partial u}\frac{\partial u}{\partial x} + \frac{\partial \tau}{\partial v}\frac{\partial v}{\partial x} = \frac{\tau_A - \tau_C}{\Delta u} J_{11} + \frac{\tau_B - \tau_C}{\Delta v} J_{21}, \\
\frac{\partial \tau}{\partial z} &= \frac{\partial \tau}{\partial u}\frac{\partial u}{\partial z} + \frac{\partial \tau}{\partial v}\frac{\partial v}{\partial z} = \frac{\tau_A - \tau_C}{\Delta u} J_{12} + \frac{\tau_B - \tau_C}{\Delta v} J_{22}.
\end{aligned} \tag{17}$$

As before, we want to solve for the traveltime at node C in triangle ΔABC. Eq. (14) can be discretized as:

$$\begin{aligned}
&\left(T_{0x}(C)\tau_C + T_0(C)\left(\frac{\tau_A - \tau_C}{\Delta u} J_{11} + \frac{\tau_B - \tau_C}{\Delta v} J_{21}\right)\right)^2 + \\
&\left(T_{0z}(C)\tau_C + T_0(C)\left(\frac{\tau_A - \tau_C}{\Delta u} J_{12} + \frac{\tau_B - \tau_C}{\Delta v} J_{22}\right)\right)^2 = S^2,
\end{aligned} \tag{18}$$

And Eq. (15) can be discretized as:

$$\begin{aligned}
&\left(T_{0x}(C) + \left(\frac{\tau_A - \tau_C}{\Delta u} J_{11} + \frac{\tau_B - \tau_C}{\Delta v} J_{21}\right)\right)^2 + \\
&\left(T_{0z}(C) + \left(\frac{\tau_A - \tau_C}{\Delta u} J_{12} + \frac{\tau_B - \tau_C}{\Delta v} J_{22}\right)\right)^2 = S^2.
\end{aligned} \tag{19}$$

Eqs. (18) and (19) are quadratic equations with one unknown variable τ_C and give the following solution. The solution of Eq. (18) is

$$\tau_C = \frac{-b \pm \sqrt{b^2 - 4ac}}{2a}, \tag{20}$$

where

$$\begin{aligned}
a &= T_{0x}^2(C) + T_{0z}^2(C) + T_0^2(C)\left(J_{11}^2 + J_{12}^2 + J_{21}^2 + J_{22}^2 + 2J_{11}J_{21} + 2J_{12}J_{22}\right) - \\
&2T_0(C)[T_{0x}(C)J_{11} + T_{0x}(C)J_{21} + T_{0z}(C)J_{12} + T_{0z}(C)J_{22}], \\
b &= T_0^2(C)\left[-2\tau_A\left(J_{11}^2 + J_{12}^2\right) - 2\tau_B\left(J_{21}^2 + J_{22}^2\right) - 2(\tau_A + \tau_B)(J_{11}J_{21} + J_{12}J_{22})\right] + \\
&2T_0(C)[\tau_A(T_{0x}(C)J_{11} + T_{0z}(C)J_{12}) + \tau_B(T_{0x}(C)J_{21} + T_{0z}(C)J_{22})], \\
c &= T_0^2(C)\left[\tau_A^2\left(J_{11}^2 + J_{12}^2\right) + \tau_B^2\left(J_{21}^2 + J_{22}^2\right) + 2\tau_A\tau_B(J_{11}J_{21} + J_{12}J_{22})\right] - S^2.
\end{aligned}$$

The solution of Eq. (19) is

$$\tau_C = \frac{-b \pm \sqrt{b^2 - 4ac}}{2a}, \tag{21}$$

where

$$\begin{aligned}
a &= J_{11}^2 + J_{12}^2 + J_{21}^2 + J_{22}^2 + 2J_{11}J_{21} + 2J_{12}J_{22}, \\
b &= -2\tau_A\left(J_{11}^2 + J_{12}^2\right) - 2\tau_B\left(J_{21}^2 + J_{22}^2\right) - 2(\tau_A + \tau_B)(J_{11}J_{21} + J_{12}J_{22}) \\
&-2T_{0x}(J_{11} + J_{21}) - 2T_{0z}(J_{12} + J_{22}), \\
c &= \tau_A^2\left(J_{11}^2 + J_{12}^2\right) + \tau_B^2\left(J_{21}^2 + J_{22}^2\right) + 2\tau_A\tau_B(J_{11}J_{21} + J_{12}J_{22}) + \\
&2\tau_A(T_{0x}J_{11} + T_{0z}J_{12}) + 2\tau_B(T_{0x}J_{21} + T_{0z}J_{22}) + T_{0x}^2 + T_{0z}^2 - S^2.
\end{aligned}$$

When the equations yield real roots, regardless of whether there is one or two solutions, we must assess whether the root is viable based on the previously stated conditions. If the equation lacks real roots or the real root fails to meet the criteria, we can resort to the method of characteristics to find τ (Fomel et al., 2009; Huang and Luo, 2020; Luo and Qian, 2012). By applying this method to edges $\overrightarrow{AC}$ and $\overrightarrow{BC}$ respectively, two values of τ can be calculated: τ_{AC} and τ_{BC}. Now, let's review the formula for the characteristic method on edge $\overrightarrow{AC}$, where $\overrightarrow{AC} = (\delta x, \delta z)$, $\left|\overrightarrow{AC}\right| = L$. The formula on edge $\overrightarrow{BC}$ is analogous and will not be derived here.

The characteristic equation for Eq. (14) is:

$$\begin{cases}
\frac{\partial x}{\partial t} = 2T_0T_{0x}\tau + 2T_0^2\frac{\partial \tau}{\partial x}, \\
\frac{\partial z}{\partial t} = 2T_0T_{0z}\tau + 2T_0^2\frac{\partial \tau}{\partial z}, \\
\frac{\partial \tau}{\partial t} = \frac{\partial \tau}{\partial x}\frac{\partial x}{\partial t} + \frac{\partial \tau}{\partial z}\frac{\partial z}{\partial t},
\end{cases} \tag{22}$$

Using the first and second equations in Eq. (22), we obtain:

$$\begin{cases} \delta x = \left(2T_0T_{0x}\tau + 2T_0^2\dfrac{\partial\tau}{\partial x}\right)\delta t, \\ \delta z = \left(2T_0T_{0z}\tau + 2T_0^2\dfrac{\partial\tau}{\partial z}\right)\delta t, \end{cases} \Rightarrow \begin{cases} \tau_x = \dfrac{1}{2T_0^2}\left(\dfrac{\delta x}{\delta t} - 2T_0T_{0x}\tau\right), \\ \tau_z = \dfrac{1}{2T_0^2}\left(\dfrac{\delta z}{\delta t} - 2T_0T_{0z}\tau\right), \end{cases} \tag{23}$$

By plugging (τ_x, τ_z) into Eq. (14), we get $\delta t = \frac{L}{2T_0S}$. Then using the third equation in Eq. (22), we get $\tau = \frac{LS+\tau_A T_0}{T_0+(T_{0x}\delta x+T_{0z}\delta z)}$.

The characteristic equation for Eq. (15) is:

$$\begin{cases} \dfrac{\partial x}{\partial t} = 2T_{0x} + 2\dfrac{\partial\tau}{\partial x}, \\ \dfrac{\partial z}{\partial t} = 2T_{0z} + 2\dfrac{\partial\tau}{\partial z}, \\ \dfrac{\partial\tau}{\partial t} = \dfrac{\partial\tau}{\partial x}\dfrac{\partial x}{\partial t} + \dfrac{\partial\tau}{\partial z}\dfrac{\partial z}{\partial t}, \end{cases} \tag{24}$$

Using the first and second equations in Eq. (24), we obtain:

$$\begin{cases} \delta x = (2T_{0x} + 2\tau_x)\delta t, \\ \delta z = (2T_{0z} + 2\tau_z)\delta t, \end{cases} \Rightarrow \begin{cases} \tau_x = \dfrac{1}{2}\left(\dfrac{\delta x}{\delta t} - 2T_{0x}\right), \\ \tau_z = \dfrac{1}{2}\left(\dfrac{\delta z}{\delta t} - 2T_{0z}\right), \end{cases} \tag{25}$$

Again, by plugging (τ_x, τ_z) into Eq. (15), we get $\delta t = \frac{L}{2S}$. Then using the third equation in Eq. (24), we get $\tau = LS - T_{0x}\delta x - T_{0z}\delta z + \tau_A$.

2.2.2. Algorithm 2: FSMCT for factored eikonal equation

The process of solving factored eikonal equations using FSMCT is similar to Algorithm 1, with the main difference being the local solver. We present the complete FSMCT algorithm for factored eikonal equations as follows:

1. Initialization.

To begin, triangulate the computational domain and assign unique labels to all nodes. Then traveltime T is decomposed into two factors $T = T_0\tau$ (or $T = T_0 + \tau$). For the node where the source is located, traveltime T is set to 0, and accordingly $\tau = 1$ (or $\tau = 0$). These points remain fixed throughout the iterations. For all other nodes, initially set the traveltimes to a large positive number, which will be updated during the subsequent iterations.

2. Preprocessing.

We also select three corner points as reference points and sort all nodes according to their L_2-distances to the reference points in ascent and descent orders. We then stored the indices of these nodes in separate arrays.:

$$\begin{aligned} &S_R^+ : \text{ascentorder}, R = 1, 2, 3; \\ &S_R^- : \text{descentorder}, R = 1, 2, 3. \end{aligned} \tag{26}$$

2. Gauss-Seidel iteration.
   (1) For $R = 1, 2, 3$:
   (2) For $S = +, -$:

Using the local solver to solve the factored eikonal equation in n triangles around the current node, and obtain the solution $\tau_n, n = 1, 2, \cdots$. Using $T = T_0\tau$ (or $T = T_0 + \tau$) to recover T and select the minimum value as the traveltime for the current node.

3. Stopping rule.

If the convergence criterion $|\tau_n - \tau_{n-1}| < \varepsilon$ is satisfied, the iteration stops. And ε is a very small positive number.

3. Numerical simulations

In this section, numerical simulations are conducted to show the performance of our method for traveltime calculation. First, we consider a constant velocity model (model 1), which is discretized by different schemes, the fully acute triangle meshes and the hybrid triangle meshes. We tested the accuracy and efficiency of FSM (Qian et al., 2007), FSMCT, and factorization approaches (FSMCTM and FSMCTA) in calculating traveltime on a fully acute triangular mesh. For hybrid triangular meshes, since existing FSMs cannot directly calculate traveltime on obtuse triangles, we only compared the computational results of FSMCT and factorization approaches. Next, we use the constant-gradient model with irregular topography (model 2) to test the applicability of our method in a more challenging case, and compare the results with the analytical solution. Finally, we apply the proposed method to the complex model with irregular topography and subsurface interfaces (model 3), and compare the calculated traveltime with the wavefield snapshot to demonstrate the effectiveness of our methods.

3.1. Model 1: A constant velocity model

To test the accuracy and reliability of our method, the computation is performed inside a 1 km × 1 km regular-shaped computational domain. The velocity of the model is 1000 m/s, and the source is deployed at (500 m, 500 m). The analytical solution of traveltime is $T = \frac{\sqrt{(x-x_0)^2+(z-z_0)^2}}{v}$, where the (x, z) is the position of any point in the model and (x_0, z_0) is the position of the source. The constant-velocity model is discretized using two triangular meshing schemes: the fully acute triangle meshes (Fig. 5(a)) and the hybrid triangle meshes including acute and obtuse angles (Fig. 5(b)).

In Fig. 5(a), we use acute triangular meshes to discretize the model, resulting in 5836 elements and 3019 nodes. The mesh exhibits high element quality, with most triangles being nearly equilateral and spatially well organized. We then separately apply the FSM proposed by Qian et al. (2007) and our FSMCT to calculate the traveltime. The results are presented in Fig. 6. Specifically, Fig. 6(a) and (b) display the traveltime contours obtained by FSM (purple lines) and FSMCT (green dashed lines). We observe that both methods can effectively solve the eikonal equation to yield the seismic traveltime, and their traveltime contours overlap. To further validate the computational accuracy of both methods, we generate error maps (Fig. 6(c) and (d)), which are identical for both FSM and FSMCT. The maximum error between the analytical traveltime and the traveltimes calculated by either FSM or FSMCT is 1.36×10^{-2}.

Upon analyzing the error maps (Fig. 6(c) and (d)), we notice distinct variations in the traveltime errors on the upper and lower flanks of the source, indicated by the red and black arrows. To elaborate on the causes of these differences, we magnify the triangular elements in the vicinity of the source (Fig. 7) and

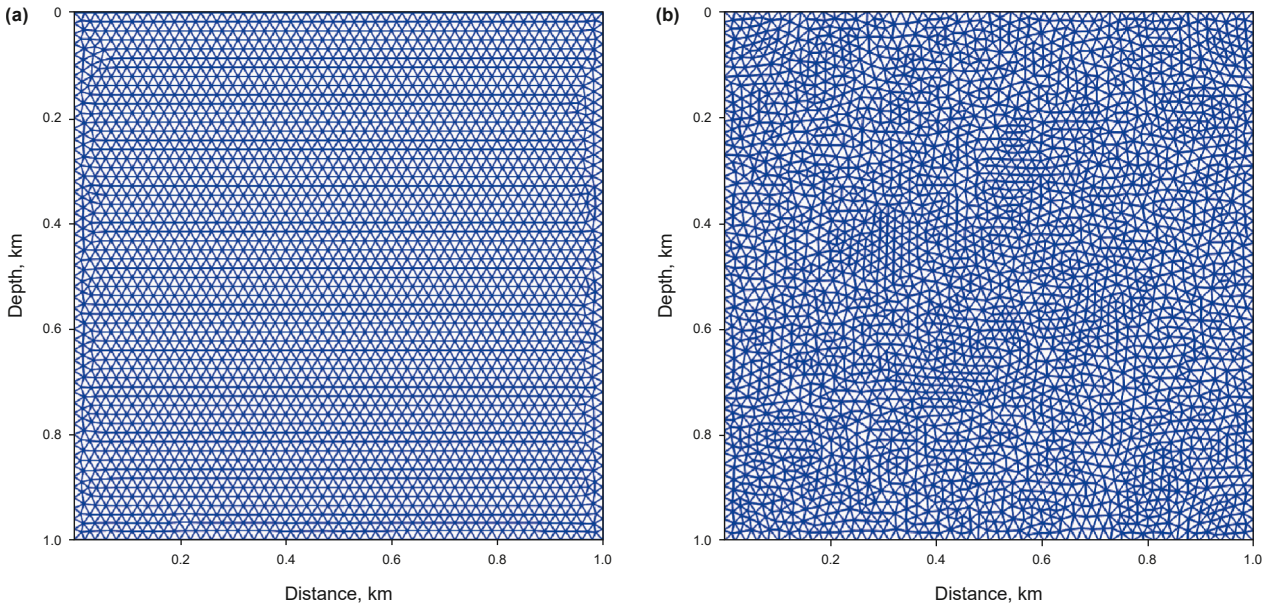

Fig. 5. Triangulation of the square model. **(a)** Acute triangular mesh. **(b)** Hybrid triangle mesh consisting of both acute and obtuse triangles.

compute the traveltime at several key nodes. The nodes A, B and C are the nodes of the triangle where the source is located, and the traveltimes can be accurately calculated: $T_A = 0.1503$ s, $T_B = 0.1026$ s, and $T_C = 0.1026$ s. The traveltime at nodes E and F is calculated along the edges AE and AF to 0.3235 s. The analytical solution at nodes E and F is 0.3386 s, and the percentage error is around 4.67%. In reality, seismic waves propagate in the form of spherical wave (the green line), and the analytical solution at point D is 0.1962 s. The eikonal solver approximates the wavefront by a plane wave (the green-dashed line) and the numerical solution of T_D is 0.2758 s, with the percentage error of around 40%. The errors caused by source singularity also exist in triangular meshes, and the error will propagate to the entire computational domain, affecting traveltime calculation accuracy. Therefore, it is necessary to eliminate the error caused by point-source singularity.

Fig. 6(a), (b) also show traveltime contours obtained by the FSMCTM and FSMCTA (as shown by the blue-dashed and black-dashed lines). The comparison clearly shows that FSMCTM and FSMCTA effectively eliminate the errors caused by the point-source singularity, and the results are closer to analytical solutions. Fig. 6(e), (f) show the traveltime errors using the FSMCTM and FSMCTA, further confirming these observations. The factored approaches (FSMCTM and FSMCTA) obviously eliminate errors around the source, and their traveltime errors are much smaller than those of FSM.

In order to further compare the accuracy and efficiency of different methods, also calculated the traveltime on acute triangular meshes of different sizes. For brevity, only the summarized results are presented in Table 1. Table 1 provides a comparison of the maximum error, mean error, and computational time for each method across different mesh sizes. The mean error is calculated as

$$\text{Error} = \frac{\sum_{i=1}^{m} |t_{\text{ana}} - t_{\text{num}}|}{m} \tag{27}$$

where t_{ana} is the analytical solution, t_{num} is the numerical solution, and m is the number of nodes. It is clear that the maximum and mean errors produced by FSMCTM and FSMCTA are smaller than those obtained by FSM and FSMCT, and that FSM and FSMCT yield identical errors. In addition, we compare the consuming time for different methods. The FSM takes time 2.53 s to reach maximum error of 5.90×10^{-3} on the 34504 triangular meshes, and the FSMCT takes time 5.08 s to reach same maximum error. In contrast, the FSMCTA takes time 0.26 s to reach maximum error of 1.09×10^{-3} on the 1470 meshes; and the FSMCTM takes time 0.31 s to reach maximum error of 1.02×10^{-3}. To reach the same accuracy level, the factored approaches require significantly less computational cost.

In Fig. 5(b), the triangular mesh exhibits lower quality, containing a mixture of acute and obtuse triangles with a more irregular spatial distribution. This mesh consists of 5826 elements and 3010 nodes. We analyze the accuracy of various solutions based on the dissection scheme in Fig. 5(b). Fig. 8(a), (b) display the traveltime contour obtained by different methods (FSMCT, FSMCTM, and FSMCTA). Compared with the FSMCT (green-dashed line), the traveltimes computed by FSMCTM (blue-dashed lines) and FSMCTA (black-dashed lines) are noticeably closer to the analytical solution. Fig. 8(c)–(e) show the traveltime difference between analytical and numerical solutions. Fig. 8(c) shows the traveltime difference for the FSMCT. Due to the singularity of the source, the error near the source is significant and exists throughout the whole computational domain. As shown in Fig. 8(d) and (e), the errors produced by FSMCTM and FSMCTA are significantly reduced, indicating that the factored approaches can deal with source singularity better in any triangular mesh. Table 2 shows maximum error, mean error, and consuming times of different methods. A comparison of the errors in Tables 1 and 2 shows that, for approximately the same number of elements, lower-quality triangular meshes tend to produce slightly larger errors. This demonstrates that numerical accuracy is affected by mesh quality.

3.2. Model 2: A constant-gradient velocity model with irregular topography

We test the proposed method on the constant gradient velocity model with an irregular surface to demonstrate its ability to

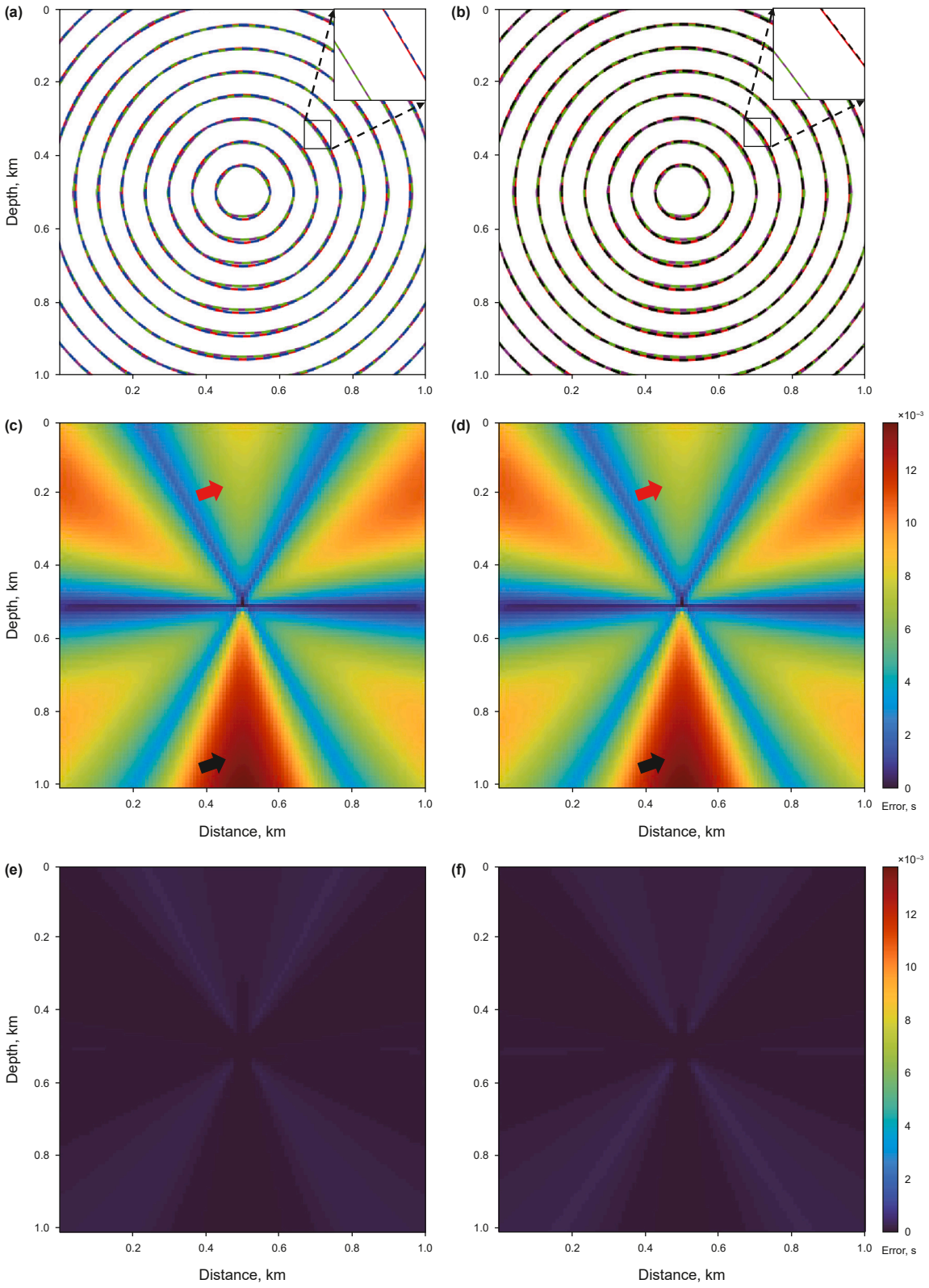

Fig. 6. Traveltime calculation and errors based on acute triangular meshes. **(a)** and **(b)** Traveltimes calculated by different method. Red: analytical solution; Purple: FSM; Green-dashed: FSMCT; Blue-dashed: FSMCTM; Black-dashed: FSMCTA. **(c)**–**(f)** Traveltime errors for FSM, FSMCT, FSMCTM and FSMCTA, respectively. The FSMCTM and FSMCTA eliminate errors caused by point source singularity, effectively improving the calculation accuracy of traveltime.

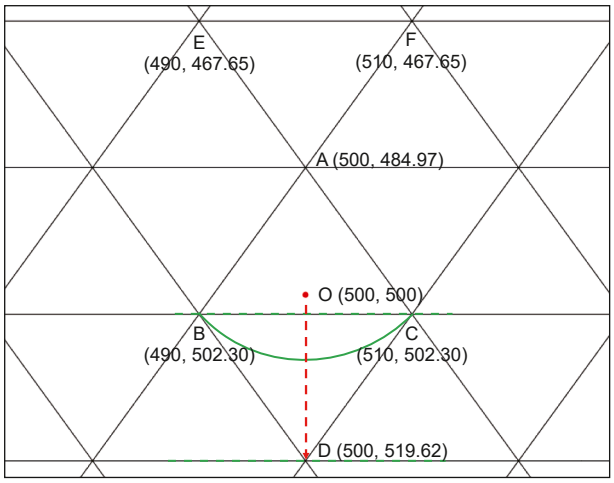

Fig. 7. Schematic diagram of triangular meshes near the source. The point O represents the source, and the traveltime is set to 0 s.

FSMCTM's performance is superior to that of FSMCTA, although its higher algebraic complexity. Fig. 10(c)–(e) show the traveltime difference between analytical and numerical solutions, with the errors showing similar characteristics as previously discussed. The factored approaches (FSMCTM and FSMCTA) can effectively eliminate the source singularity and improve the calculation accuracy of traveltime in the complex model.

3.3. Model 3: Complex model with irregular topography and subsurface interfaces

We evaluate our method using unstructured triangular meshes on the cropped foothill model shown in Fig. 11, which features rugged topography and irregular subsurface interfaces. This model spans 7.2 km in width and 3.2 km in depth, with velocity values ranging from 3700 to 5100 m/s. The solid black line in Fig. 11 outlines the topography, exhibiting a maximum elevation difference of 1090 m. The source is situated at the surface, marked by a red pentagram, with coordinates at (3.6 km, 0.56 km), as indicated

Table 1
Errors and computational time of different methods for Model 1 with varying mesh sizes.

The number of triangles		1470	5836	16370	34504
The number of nodes		786	3019	8354	17497
FSM	Maximum error	2.06×10^{-2}	1.36×10^{-2}	7.98×10^{-3}	5.90×10^{-3}
	Mean error	1.07×10^{-2}	6.54×10^{-3}	4.22×10^{-3}	3.14×10^{-3}
	Time, s	0.23	0.52	1.41	2.53
FSMCT	Maximum error	2.06×10^{-2}	1.36×10^{-2}	7.98×10^{-3}	5.90×10^{-3}
	Mean error	1.07×10^{-2}	6.54×10^{-3}	4.22×10^{-3}	3.14×10^{-3}
	Time, s	0.24	0.86	2.44	5.08
FSMCTA	Maximum error	1.09×10^{-3}	3.76×10^{-4}	2.89×10^{-4}	1.59×10^{-4}
	Mean error	4.61×10^{-4}	1.19×10^{-4}	9.66×10^{-5}	7.78×10^{-5}
	Time, s	0.26	1.28	6.51	16.94
FSMCTM	Maximum error	1.02×10^{-3}	3.03×10^{-4}	2.76×10^{-4}	1.56×10^{-4}
	Mean error	3.87×10^{-4}	1.14×10^{-4}	8.62×10^{-5}	7.69×10^{-5}
	Time, s	0.31	1.44	7.27	19.33

handle complex topographies. The model is shown in Fig. 9(a), the slowness can be expressed as:

$$\frac{1}{s(x,z)} = \frac{1}{s_O(x,z)} + G_0 \cdot (x - x_O, z - z_O),$$

where the $s_O(x,z)$ is the slowness at the source (x_O, z_O), and G_0 is constant gradient of velocity. The analytical solution of traveltime can be written as (Huang et al., 2019; Treister and Haber, 2016):

$$T = \frac{1}{G_0} \operatorname{arccosh}\left(1 + \frac{1}{2} s(x,z) s_O(x,z) |G_0|^2 |(x,z) - (x_O, z_O)|^2\right),$$

where the source is located at $x_O = 0.5$ km and $z_O = 0.5$ km, and we set $G_0 = (0, 0.5)$ in the example. Fig. 9(b) shows the triangular mesh composed of 5696 triangular elements, which can effectively handle irregular surfaces.

Fig. 10(a) and (b) compare the traveltime contours obtained for the FSMCT and the factored approaches. The figure shows that three methods based on triangular meshes can effectively calculate seismic traveltime in the model with irregular interface. Due to the singularity of the point source, there is a significant error between the traveltime calculated by FSMCT and the analytical solution. The traveltime contours obtained by FSMCTM and FSMCTA agree better with the analytical solution, and the enlarged image in the upper right corner can better exhibit the performance of the factored approaches. Further comparison shows that

by a red pentagram. Fig. 12 illustrates the triangulation of each region, tailored to the subsurface interfaces, resulting in meshes composed of 38373 triangles of varying sizes. This demonstrates that unstructured triangular meshes can effectively adapt to irregular interfaces, enabling precise meshing of complex models.

The traveltime contours obtained by different methods are superimposed over the complex model in Fig. 13. It is clearly observed that the results obtained by the three methods are relatively close, and the contours show the obvious tortuous shape in areas with drastic velocity changes. To further illustrate the quality of the result, we use the discontinuous Galerkin method to solve the acoustic equation on the same triangle meshes and obtain wavefield snapshots (He et al., 2020; He and Yue, 2019). In Fig. 14, the traveltime contours obtained by the three methods are superimposed over the wavefield snapshots at 0.5 s and 0.7 s and visually observe that the traveltime contours match the wavefront. Our proposed methods have proven to calculate traveltime effectively in complex models. For further comparison, we enlarged the local area and found that the results of FSMCTM and FSMCTA are more consistent with the wavefront. After eliminating point source singularity, the calculation accuracy of traveltime has improved.

To further demonstrate the superiority of triangular meshes over rectangular meshes in adapting to complex models, we conducted a set of comparative experiments based on different mesh sizes. For the triangular meshes, we compute the traveltimes

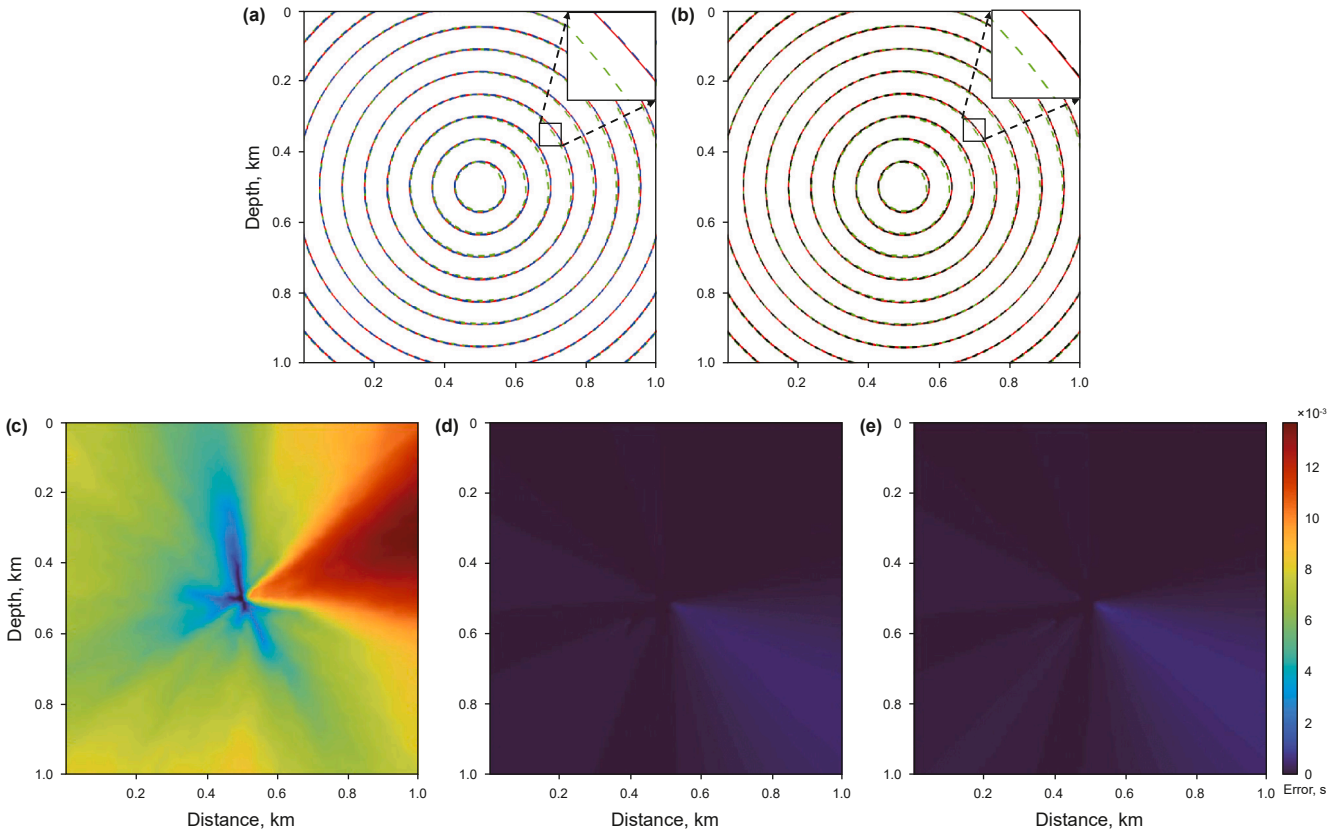

Fig. 8. Traveltime calculation and errors based on complex triangular meshes. **(a)**–**(b)** Traveltimes calculated by different methods. Red-curve: analytical solution; green-dashed: FSMCT; blue-dashed: FSMCTM; black-dashed: FSMCTA. **(c)**–**(e)** Traveltime errors for FSMCT, FSMCTM and FSMCTA, respectively.

Table 2
Maximum error, mean error, and computational time of different methods.

	Maximum error	Mean error	Time, s
FSMCT	1.37×10^{-2}	7.38×10^{-3}	0.85
FSMCTA	7.99×10^{-4}	1.58×10^{-4}	1.07
FSMCTM	5.42×10^{-4}	1.58×10^{-4}	1.25

using the FSMCT, whereas for the rectangular meshes, the conventional FSM (Huang and Bellefleur, 2012) is employed. In the complex structural model, where no analytical solution is available, we consider the traveltimes computed on the finest grid ($dh = 5$ m for triangular meshes and $dx = dz = 5$ m for rectangular meshes) to be the most accurate and thus use them as reference solutions. We then gradually increased the grid size to 10, 20, and 40 m, and compared the resulting traveltimes against the reference, as shown in Fig. 15. As the grid size increases, the traveltimes obtained with triangular meshes exhibit relatively small errors compared with the reference solution, whereas the traveltimes computed on rectangular grids show more pronounced deviations. We attribute this discrepancy not only to the general loss of accuracy on coarser grids but also to the inability of rectangular meshes to conform to irregular geological boundaries, which introduces additional geometric errors.

To provide a quantitative assessment, we evaluate the traveltime accuracy by computing the mean error. It can be seen from Table 3 that triangular meshes consistently yield smaller errors than rectangular meshes, highlighting their advantages in computing seismic traveltimes within complex geological models. While triangular meshes demonstrate improved accuracy, their computational efficiency is significantly lower than that of structured rectangular grids, suggesting that future work should focus on developing acceleration strategies for triangular-mesh-based solvers.

4. Discussion

In this study, we proposed a novel fast sweeping method, FSMCT, to compute traveltimes in models with rugged topography and irregular subsurface interfaces. FSMCT transforms triangular elements in the physical domain into canonical reference triangles to solve the eikonal equation, thereby avoiding the subdivision of obtuse triangles required by conventional FSM. However, when the triangular mesh exhibits strong distortion or an irregular spatial arrangement, the numerical errors increase, indicating that the computational accuracy still depends, to some extent, on the quality of the mesh.

In the presented examples, the triangular mesh was constructed according to the irregular interfaces, allowing the geometry to be accurately represented. However, in traveltime tomography, the velocity field is often smooth and the subsurface interfaces are not explicitly known, in which case the advantages of triangular meshes may appear less evident. Compared with structured rectangular meshes, unstructured triangular meshes offer the advantage of adaptive refinement. They can be subdivided into smaller meshes in the simpler and more flexible manner, allowing the use of finer meshes in regions of particular interest. When the approximate locations of irregular interfaces or anomalous bodies are available, the triangular mesh can be adaptively refined in these regions, enabling more accurate

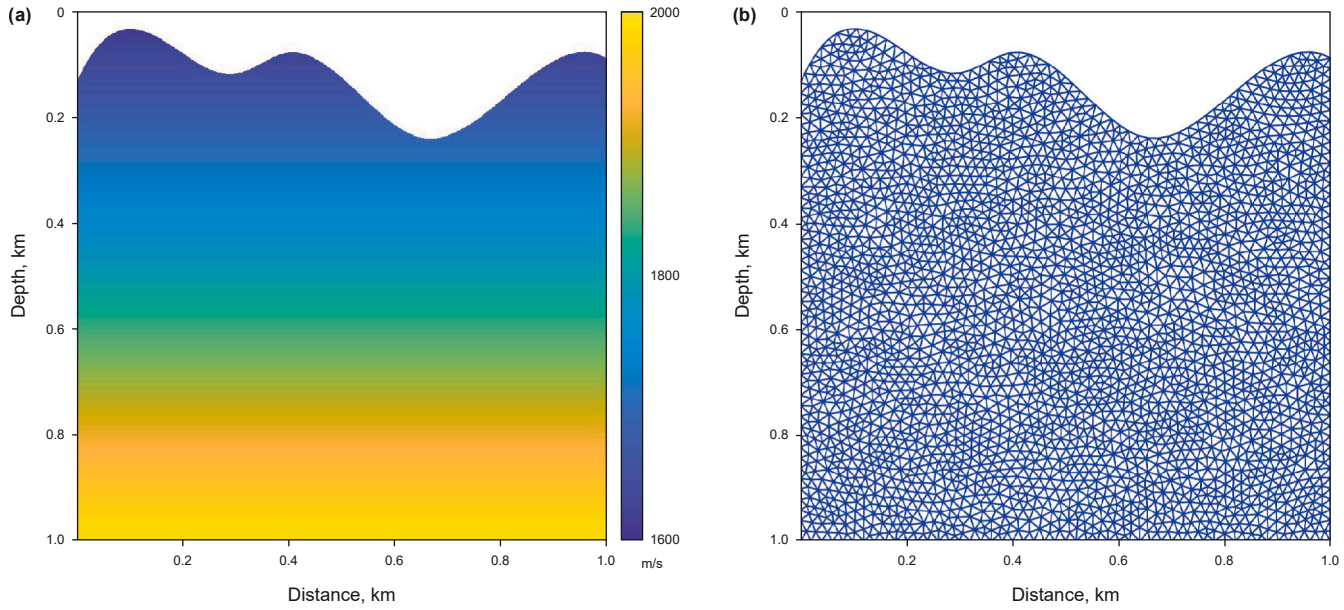

Fig. 9. (**a**) Model with irregular surface. (**b**) Triangulation of the model.

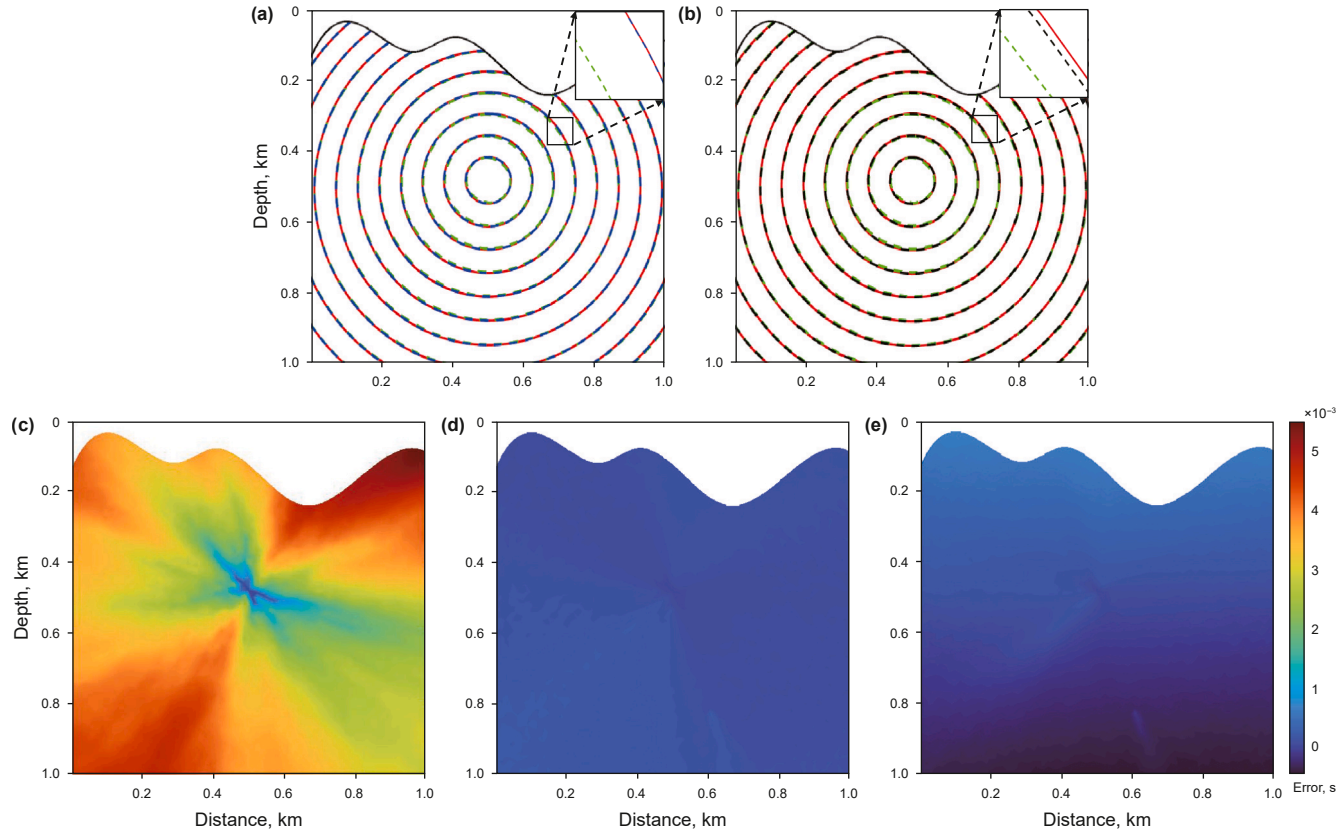

Fig. 10. (**a**) and (**b**) Traveltimes calculated by different methods. Red-curve: analytical solution; green-dashed: FSMCT; blue-dashed: FSMCTM; black-dashed: FSMCTA. Traveltime errors obtained by (**c**) FSMCT, (**d**) FSMCTM, (**e**) FSMCTA.

traveltime computation and better capturing of local structural details. Although adaptive refinement of triangular meshes has not yet been fully explored in the current study, it will be an important focus of our future research.

In addition, the present study primarily focuses on applying FSMCT to compute traveltimes in two-dimensional media. Nevertheless, the method can be extended to three-dimensional problems in a relatively straightforward manner. By adopting the

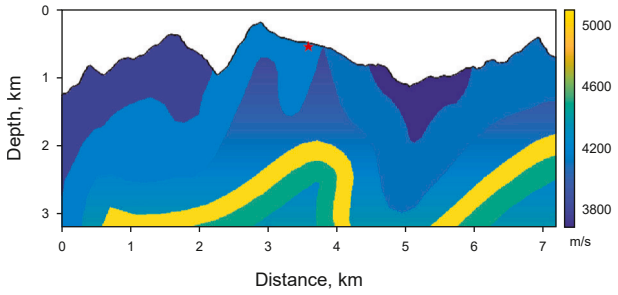

Fig. 11. Complex model with irregular topography and subsurface interfaces (the white region denotes air).

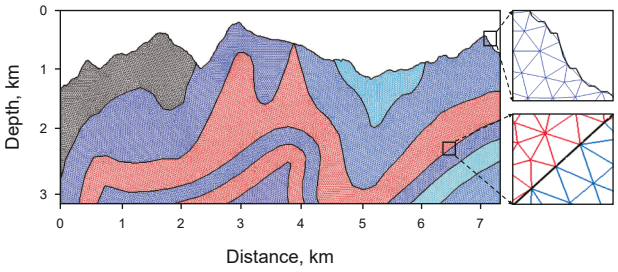

Fig. 12. Triangulation of the model following the underground velocity interfaces. A zoomed-in view of the local mesh shows that the unstructured triangular meshes can accurately depict the irregular geometry.

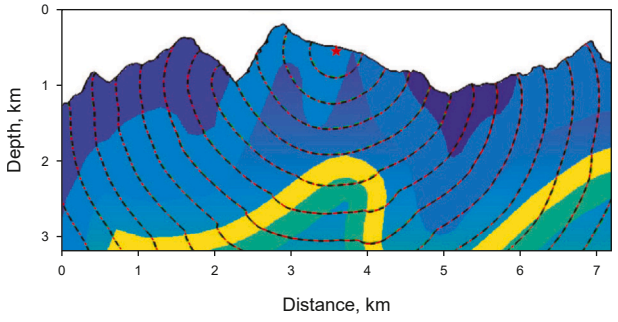

Fig. 13. Traveltimes calculated by different methods. Green-dashed: FSMCT; red-dashed: FSMCTM; black-dashed: FSMCTA.

idea of coordinate transformation, irregular tetrahedral elements can be mapped to a reference tetrahedron, and the eikonal equation can then be solved using finite-difference schemes to obtain traveltimes. However, several challenges are anticipated in such an extension. First, generating high-quality tetrahedral meshes in 3D is more complex and requires efficient and robust meshing techniques. Second, the computational cost and memory requirements will increase significantly, necessitating advanced strategies such as GPU acceleration and large-scale parallel computing. Despite these challenges, we believe that FSMCT can be effectively extended to 3D traveltime computation, and we plan to pursue this direction in our future work.

In recent years, deep learning methods have gradually demonstrated certain application potential in seismic exploration (Cha et al., 2023; Fang et al., 2025; Fu et al., 2025; Gou et al., 2023; Sun and Demanet, 2022) and have begun to be explored for solving problems related to the eikonal equation (Smith et al., 2021; Waheed et al., 2021). Based on the triangular-element discretization framework adopted in this study, future research may further

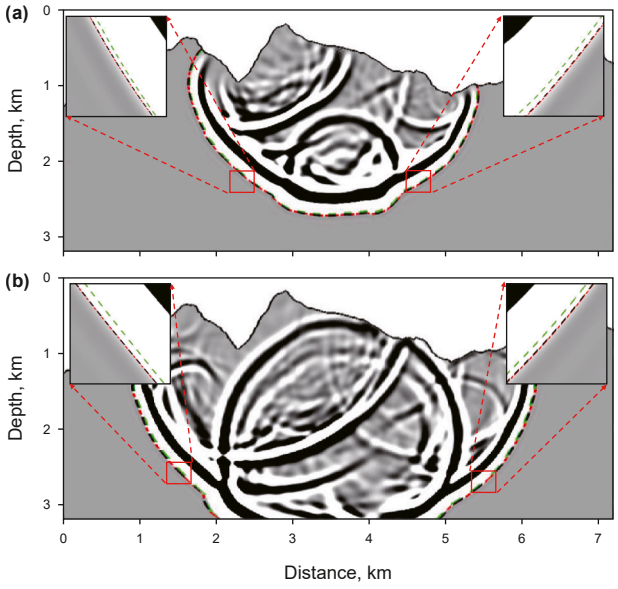

Fig. 14. Wavefield snapshots of the complex model at **(a)** $t = 0.5$ s and **(b)** $t = 0.7$ s. Traveltime contours from FSMCT (green-dashed), FSMCTM (red-dashed), and FSMCTA (black-dashed) are superimposed.

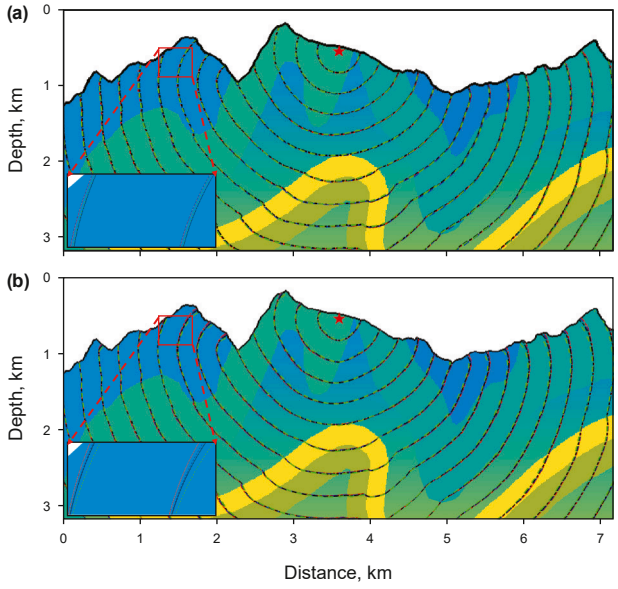

Fig. 15. Traveltimes computed on **(a)** triangular meshes and **(b)** rectangular meshes with different grid sizes. The red, yellow, blue, and green contours correspond to traveltimes obtained with mesh sizes of 5, 10, 20, and 40 m, respectively. Enlarged views of the corner region highlight that the traveltimes calculated with triangular meshes are closer to the reference solution.

Table 3
The numerical error of different mesh sizes.

Size, m	Mesh	
	Triangle	Rectangle
10	6.45×10^{-4}	0.0016
20	0.0018	0.0041
40	0.0032	0.0085

investigate the feasibility of integrating triangular-element methods with deep learning techniques as a potential direction for extension.

5. Conclusion

In this study, we have introduced the FSMCT on unstructured triangular meshes, providing a robust tool for calculating traveltimes in models with irregular geometries. FSMCT leverages the concept of coordinate transformation to map physical triangles onto standard reference triangles and constructs an upwind difference scheme on the reference triangle to solve the eikonal equation. This approach allows FSMCT to be readily extended to tackle the factored eikonal equation, effectively eliminating errors stemming from point source singularities, thus enhancing the accuracy of traveltime calculations. Our method can compute traveltimes for any physical triangle, eliminating the need for reprocessing obtuse triangles. Numerical tests highlight the effectiveness and precision of our approach in models featuring irregular topographies and subsurface interfaces.

CRediT authorship contribution statement

Xin Chen: Visualization, Project administration, Methodology, Formal analysis. **Dan-Ping Cao:** Supervision, Methodology. **Zhao-Lin Zhu:** Formal analysis. **Xin Fu:** Methodology, Investigation, Formal analysis, Conceptualization.

Declaration of competing interest

The authors declare no conflict of interest.

Acknowledgements

This work was supported by the National Natural Science Foundation of China (42325403, 42074162). Xin Fu was additionally supported by the National Natural Science Foundation of China (No. 42504116), the Deep Earth Probe and Mineral Resources Exploration - National Science and Technology Major Project (No. 2024ZD1004201), the Young Expert of Taishan Scholars Project (No. tsqn202408095).

APPENDIX A. Detailed process of solving the characteristic equation to obtain τ

Here, we provide a detailed derivation of the formula for calculating τ using the characteristic method. Applying the method to the edges $\overrightarrow{AC}$ and $\overrightarrow{BC}$, the value of τ at point C can be derived respectively. Now, let's review the formula for the characteristic method on edge $\overrightarrow{AC}$, where $\overrightarrow{AC} = (\delta x, \delta z)$, $\left|\overrightarrow{AC}\right| = L$. The formula on edge $\overrightarrow{BC}$ is analogous and will not be derived here.

Eq. (22) is the characteristic equation for the multiplicatively factored eikonal equation. Using the first and second equations of Eq. (22), Eq. (23) can be obtained, which provides the expressions for τ_x and τ_z:

$$\begin{cases} \tau_x = \dfrac{1}{2T_0^2}\left(\dfrac{\delta x}{\delta t} - 2T_0 T_{0x}\tau\right), \\ \tau_z = \dfrac{1}{2T_0^2}\left(\dfrac{\delta z}{\delta t} - 2T_0 T_{0z}\tau\right), \end{cases} \tag{A1}$$

Eq. (A1) can be substituted into Eq. (14) to obtain:

$$\left(T_{0x}\tau + \frac{1}{2T_0}\left(\frac{\delta x}{\delta t} - 2T_0 T_{0x}\tau\right)\right)^2 + \left(T_{0z}\tau + \frac{1}{2T_0}\left(\frac{\delta z}{\delta t} - 2T_0 T_{0z}\tau\right)\right)^2 = S^2. \tag{A2}$$

The formula above expresses T_{0x} and T_{0z} as abbreviations for $\frac{\partial T_0}{\partial x}$ and $\frac{\partial T_0}{\partial z}$. Expanding the equation results in:

$$\begin{aligned} &\left(T_{0x}^2\tau^2 + T_{0z}^2\tau^2\right) + \frac{\left(\frac{\delta x}{\delta t}\right)^2 + (2T_0 T_{0x}\tau)^2 - 4\frac{\delta x}{\delta t}T_0 T_{0x}\tau + \left(\frac{\delta z}{\delta t}\right)^2 + (2T_0 T_{0z}\tau)^2 - 4\frac{\delta z}{\delta t}T_0 T_{0z}\tau}{4T_0^2} \\ &\quad + \frac{T_{0x}\left(\frac{\delta x}{\delta t} - 2T_0 T_{0x}\tau\right) + T_{0z}\left(\frac{\delta z}{\delta t} - 2T_0 T_{0z}\tau\right)}{T_0}\tau = S^2. \end{aligned} \tag{A3}$$

After simplification, the result is:

$$\begin{aligned} &4T_0^2\left(T_{0x}^2 + T_{0z}^2\right)\tau^2 + \left(\frac{\delta x}{\delta t}\right)^2 + \left(\frac{\delta z}{\delta t}\right)^2 + 4T_0^2\tau^2\left(T_{0x}^2 + T_{0z}^2\right) \\ &- 8T_0^2\tau^2\left(T_{0x}^2 + T_{0z}^2\right) = 4T_0^2 S^2. \end{aligned} \tag{A4}$$

Further simplification yields:

$$\frac{(\delta x)^2 + (\delta z)^2}{(\delta t)^2} = 4T_0^2 S^2. \tag{A5}$$

Since $(\delta x)^2 + (\delta z)^2 = L^2$, it follows that:

$$\delta t = \frac{L}{2T_0 S}. \tag{A6}$$

Now, we can calculate the value of τ at point C using the third equation of Eq. (22) through edge $\overrightarrow{AC}$. By manipulating the equation, we obtain:

$$\frac{\tau_C - \tau_A}{\delta t} = \tau_x\frac{\delta x}{\delta t} + \tau_z\frac{\delta z}{\delta t}. \tag{A7}$$

Substituting the expressions for τ_x, τ_z, and δt into Eq. (A7) gives:

$$\tau_C - \tau_A = \frac{1}{2T_0^2}\left(\frac{\delta x}{\frac{L}{2T_0 S}} - 2T_0 T_{0x}\tau_C\right)\delta x + \frac{1}{2T_0^2}\left(\frac{\delta z}{\frac{L}{2T_0 S}} - 2T_0 T_{0z}\tau_C\right)\delta z, \tag{A8}$$

Simplifying Eq. (A8) yields:

$$(\tau_C-\tau_A)2T_0^2\frac{L}{2T_0S}=(\delta x)^2+(\delta z)^2-2T_0T_{0x}\tau_C\delta x\frac{L}{2T_0S}-2T_0T_{0z}\tau_C\delta z\frac{L}{2T_0S}, \tag{A9}$$

Since $(\delta x)^2+(\delta z)^2=L^2$, it follows that:

$$(\tau_C-\tau_A)2T_0^2\frac{L}{2T_0S}=L^2-2T_0T_{0x}\tau_C\delta x\frac{L}{2T_0S}-2T_0T_{0z}\tau_C\delta z\frac{L}{2T_0S}, \tag{A10}$$

Finally, the value of τ at point C can be obtained as:

$$\tau_C=\frac{LS+T_0\tau_A}{T_0+T_{0x}\delta x+T_{0z}\delta z}. \tag{A11}$$

Next, we present the detailed formulas corresponding to the characteristic method of the additively factored eikonal equation. From the first and second equations of Eq. (24), the expressions for τ_x and τ_z can be obtained as:

$$\begin{cases}\tau_x=\frac{1}{2}\left(\frac{\delta x}{\delta t}-2T_{0x}\right),\\ \tau_z=\frac{1}{2}\left(\frac{\delta z}{\delta t}-2T_{0z}\right),\end{cases} \tag{A12}$$

and Eq. (A12) can be substituted into Eq. (15) to obtain:

$$\left(T_{0x}+\frac{1}{2}\left(\frac{\delta x}{\delta t}-2T_{0x}\right)\right)^2+\left(T_{0z}+\frac{1}{2}\left(\frac{\delta z}{\delta t}-2T_{0z}\right)\right)^2=S^2, \tag{A13}$$

The formula above expresses T_{0x} and T_{0z} as abbreviations for $\frac{\partial T_0}{\partial x}$ and $\frac{\partial T_0}{\partial z}$. Expanding this equation results in:

$$(T_{0x})^2+(T_{0z})^2+\frac{\left(\frac{\delta x}{\delta t}-2T_{0x}\right)^2+\left(\frac{\delta z}{\delta t}-2T_{0z}\right)^2}{4}+T_{0x}\left(\frac{\delta x}{\delta t}-2T_{0x}\right)+T_{0z}\left(\frac{\delta z}{\delta t}-2T_{0z}\right)=S^2, \tag{A14}$$

After simplification, the result is:

$$\frac{1}{4}\left(\frac{\delta x}{\delta t}\right)^2+\frac{1}{4}\left(\frac{\delta z}{\delta t}\right)^2=S^2, \tag{A15}$$

Since $(\delta x)^2+(\delta z)^2=L^2$, it follows that:

$$\delta t=\frac{L}{2S}. \tag{A16}$$

Now, we can calculate the value of τ at point C using the third equation of Eq. (24) through edge $\overrightarrow{AC}$. By manipulating the equation, we obtain:

$$\frac{\tau_C-\tau_A}{\delta t}=\tau_x\frac{\delta x}{\delta t}+\tau_z\frac{\delta z}{\delta t} \tag{A17}$$

Substituting the expressions for τ_x, τ_z, and δt into the third Eq. (A17) gives:

$$\tau_C-\tau_A=\frac{1}{2}\left(\frac{\delta x}{\frac{L}{2S}}-2T_{0x}\right)\delta x+\frac{1}{2}\left(\frac{\delta z}{\frac{L}{2S}}-2T_{0z}\right)\delta z, \tag{A18}$$

Simplifying Eq. (A18) yields:

$$\tau_C-\tau_A=\left(\frac{\delta x}{L}S-T_{0x}\right)\delta x+\left(\frac{\delta z}{L}S-T_{0z}\right)\delta z, \tag{A19}$$

Based on $(\delta x)^2+(\delta z)^2=L^2$, the value of τ at point C can be obtained as:

$$\tau_C=LS-\delta xT_{0x}-\delta zT_{0z}+\tau_A. \tag{A20}$$

References

Bai, C., Huang, G., Zhao, R., 2010. 2-D/3-D irregular shortest-path ray tracing for multiple arrivals and its applications. Geophys. J. Int. 183 (3), 1596–1612. https://doi.org/10.1111/j.1365-246X.2010.04817.x.

Barth, T.J., Sethian, J.A., 1998. Numerical schemes for the Hamilton–Jacobi and level set equations on triangulated domains. J. Comput. Phys. 145 (1), 1–40. https://doi.org/10.1006/jcph.1998.6007.

Cha, Y.-J., Mostafavi, A., Benipal, S.S., 2023. DNoiseNet: Deep learning-based feedback active noise control in various noisy environments. Eng. Appl. Artif. Intell. 121, 105971. https://doi.org/10.1016/j.engappai.2023.105971.

Cheng, C., Bodin, T., Allen, R.M., 2016. Three-dimensional pre-stack depth migration of receiver functions with the fast marching method: A Kirchhoff approach. Geophys. J. Int. 205 (2), 819–829. https://doi.org/10.1093/gji/ggw062.

Cordier, S., Goudon, T., GutnicDumbser, M., et al., 2005. Numerical Methods for Hyperbolic and Kinetic Problems. EMS Press, Berlin, Germany, pp. 295–333 doi:OI10.4171/012.

Fang, J., Wang, N., Zhao, P., Wang, E., Shen, H., 2025. Deep learning reparameterized FWI using a frequency-normalized gradient. IEEE Geosci. Remote Sens. Lett. 22, 7509905. https://doi.org/10.1109/LGRS.2025.3624703.

Fomel, S., Luo, S., Zhao, H., 2009. Fast sweeping method for the factored eikonal equation. J. Comput. Phys. 228 (17), 6440–6455. https://doi.org/10.1016/j.jcp.2009.05.029.

Fu, X., Cao, D., Zhang, F., 2025. Deep-learning-based denoising of prestack seismic angle gathers with application to time-lapse data. Geophysics 91 (1), WA11–WA21. https://doi.org/10.1190/geo2024-0472.1.

Fu, Z., Jeong, W.-K., Pan, Y., Kirby, R.M., Whitaker, R.T., 2011. A fast iterative method for solving the eikonal equation on triangulated surfaces. SIAM J. Sci. Comput. 33 (5), 2468–2488. https://doi.org/10.1137/100788951.

Gou, R., Zhang, Y., Zhu, X., Gao, J., 2023. Bayesian physics-informed neural networks for the subsurface tomography based on the eikonal equation. IEEE Trans. Geosci. Rem. Sens. 61, 4503012. https://doi.org/10.1109/TGRS.2023.3286438.

Hassouna, M.S., Farag, A.A., 2007. MultiStencils fast marching methods: A highly accurate solution to the eikonal equation on Cartesian domains. IEEE Trans. Pattern Anal. Mach. Intell. 29 (9), 1563–1574. https://doi.org/10.1109/TPAMI.2007.1154.

He, X., Yue, X., 2019. A high-order weighted runge-kutta discontinuous galerkin method for solving 2D acoustic and elastic wave equations in isotropic and anisotropic media. J. Seismic Explor. 28 (4), 363–391.

He, X., Yang, D., Huang, X., Ma, X., 2020. A numerical dispersion-dissipation analysis of discontinuous Galerkin methods based on quadrilateral and triangular elements. Geophysics 85 (3), T101–T121. https://doi.org/10.1190/geo2019-0109.1.

Huang, G., Luo, S., 2020. Hybrid fast sweeping methods for anisotropic eikonal equation in two-dimensional tilted transversely isotropic media. J. Sci. Comput. 84 (2), 32. https://doi.org/10.1007/s10915-020-01280-3.

Huang, G., Hu, Q., Luo, S., Li, H., Zhang, H., Nobes, D.C., 2019. 2-D fast sweeping method for the factored Eikonal equation and its improvement on inversion accuracy. J. Appl. Geophys. 166, 68–76. https://doi.org/10.1016/j.jappgeo.2019.04.016.

Huang, J., Bellefleur, G., 2012. Joint transmission and reflection traveltime tomography using the fast sweeping method and the adjoint-state technique. Geophys. J. Int. 188 (2), 570–582. https://doi.org/10.1111/j.1365-246X.2011.05273.x.

Jacquet, P., 2021. Time-Domain Full Waveform Inversion Using Advanced Discontinuous Galerkin Method. Theses, Universite de Pau Et des Pays de l'Adour.

Käser, M., Dumbser, M., 2006. An arbitrary high-order discontinuous Galerkin method for elastic waves on unstructured meshes—I. The two-dimensional isotropic case with external source terms. Geophys. J. Int. 166 (2), 855–877. https://doi.org/10.1111/j.1365-246X.2006.03051.x.

Kimmel, R., Sethian, J.A., 1998. Computing geodesic paths on manifolds. Proc. Natl. Acad. Sci. 95 (15), 8431–8435. https://doi.org/10.1073/pnas.95.15.8431.

Li, B., Liu, G.F., Liu, H., 2009. A method of using GPU to accelerate seismic pre-stack time migration. Chin. J. Geophys. 52 (1), 242–249. https://doi.org/10.1002/cjg2.1345.

Li, Y., Zhang, G., Hu, G., Li, K., Luo, Y., Liang, C., Duan, J., 2023. High-precision and high-efficiency first-arrival slope tomography via eikonal solvers and the adjoint-state method. J. Geophys. Eng. 20 (4), 774–787. https://doi.org/10.1093/jge/gxad051.

Luo, S., Qian, J., 2012. Fast sweeping methods for factored anisotropic eikonal equations: Multiplicative and additive factors. J. Sci. Comput. 52 (2), 360–382. https://doi.org/10.1007/s10915-011-9550-y.
Qian, J., Zhang, Y.T., Zhao, H.K., 2007. Fast sweeping methods for eikonal equations on triangular meshes. SIAM J. Numer. Anal. 45 (1), 83–107. https://doi.org/10.1137/050627083.
Qiao, B.-P., Li, Q.-Q., He, W.-G., Zhao, D., Wu, Q.-B., 2024. An adaptive finite-difference method for seismic traveltime modeling based on 3D eikonal equation. Pet. Sci. 21 (1), 195–205. https://doi.org/10.1016/j.petsci.2023.09.013.
Qiu, C., Yang, D., He, X., Li, J., 2020. A weighted Runge-Kutta discontinuous Galerkin method for reverse time migration. Geophysics 85 (6), S343–S355. https://doi.org/10.1190/geo2019-0193.1.
Rawlinson, N., Sambridge, M., 2004. Multiple reflection and transmission phases in complex layered media using a multistage fast marching method. Geophysics 69 (5), 1338–1350. https://doi.org/10.1190/1.1801950.
Rawlinson, N., Kool, M.d., Sambridge, M., 2006. Seismic wavefront tracking in 3D heterogeneous media: applications with multiple data classes. Explor. Geophys. 37, 322–330.
Sambolian, S., Operto, S., Ribodetti, A., Tavakoli F, B., Virieux, J., 2019. Parsimonious slope tomography based on eikonal solvers and the adjoint-state method. Geophys. J. Int. 218 (1), 456–478. https://doi.org/10.1093/gji/ggz150.
Schall, E., Leservoisier, D., Dervieux, A., Koobus, B., 2004. Mesh adaptation as a tool for certified computational aerodynamics. Int. J. Numer. Methods Fluid. 45, 179–196. https://doi.org/10.1002/fld.642.
Sethian, J.A., 1999. Fast marching methods. SIAM Rev. 41 (2), 199–235. https://doi.org/10.1137/s0036144598347059.
Sethian, J.A., Popovici, A.M., 1999. 3-D traveltime computation using the fast marching method. Geophysics 64 (2), 516–523. https://doi.org/10.1190/1.1444558.
Smith, J.D., Azizzadenesheli, K., Ross, Z.E., 2021. EikoNet: solving the eikonal equation with deep neural networks. IEEE Trans. Geosci. Rem. Sens. 59 (12), 10685–10696. https://doi.org/10.1109/TGRS.2020.3039165.
Sun, H., Demanet, L., 2022. Deep learning for low-frequency extrapolation of multicomponent data in elastic FWI. IEEE Trans. Geosci. Rem. Sens. 60, 1–11. https://doi.org/10.1109/TGRS.2021.3135790.
Tavakoli, F.B., Ribodetti, A., Virieux, J., Operto, S., 2015. An Iterative Factored Eikonal Solver for TTI Media, 2015. SEG Technical Program Expanded Abstracts 2015, pp. 3576–3581.
Tavakoli, F.B., Operto, S., Ribodetti, A., Virieux, J., 2017. Slope tomography based on eikonal solvers and the adjoint-state method. Geophys. J. Int. 209 (3), 1629–1647. https://doi.org/10.1093/gji/ggx111.
Treister, E., Haber, E., 2016. A fast marching algorithm for the factored eikonal equation. J. Comput. Phys. 324, 210–225. https://doi.org/10.1016/j.jcp.2016.08.012.
Vidale, J., 1988. Finite-difference calculation of travel times. Bull. Seismol. Soc. Am. 78 (6), 2062–2076. https://doi.org/10.1785/bssa0780062062.
Vidale, J.E., 1990. Finite-difference calculation of traveltimes in three dimensions. Geophysics 55 (5), 521–526. https://doi.org/10.1190/1.1442863.
Waheed, U., Haghighat, E., Alkhalifah, T., Song, C., Hao, Q., 2021. PINNeik: Eikonal solution using physics-informed neural networks. Comput. Geosci. 155, 104833. https://doi.org/10.1016/j.cageo.2021.104833.
Wang, T.-F., Cheng, J.-B., Geng, J.-H., 2022. Reflection-based traveltime and waveform inversion with second-order optimization. Pet. Sci. 19 (4), 1582–1591. https://doi.org/10.1016/j.petsci.2022.02.003.
Xin, H., Zhang, H., Kang, M., He, R., Gao, L., Gao, J., 2018. High-Resolution lithospheric velocity structure of Continental China by double-difference seismic travel-time tomography. Seismol Res. Lett. 90 (1), 229–241. https://doi.org/10.1785/0220180209.
Xu, T., Xu, G., Gao, E., Li, Y., Jiang, X., Luo, K., 2006. Block modeling and segmentally iterative ray tracing in complex 3D media. Geophysics 71 (3), T41–T51. https://doi.org/10.1190/1.2192948.
Zhang, Q., Ma, X., Nie, Y., 2021. An iterative fast sweeping method for the eikonal equation in 2D anisotropic media on unstructured triangular meshes. Geophysics 86 (3), U49–U61. https://doi.org/10.1190/geo2020-0187.1.
Zhang, Q., Ma, X., Nie, Y., 2023a. Eikonal equation-based earthquake location with irregular surfaces. Geophys. J. Int. 234 (1), 136–152. https://doi.org/10.1093/gji/ggad051.
Zhang, Q., Nie, Y., Ma, X., 2023b. An efficient hybrid mesh method for seismic traveltime computation with irregular surfaces. J. Appl. Geophys. 209, 104905. https://doi.org/10.1016/j.jappgeo.2022.104905.
Zhao, C., Zhang, L., Yu, P., Liu, Y., Feng, S., 2019. Combined inversion of first-arrival travel times and reflection travel times. Geophys. Prospect. 67 (7), 1764–1777. https://doi.org/10.1111/1365-2478.12791.
Zhao, D., Hasegawa, A., Horiuchi, S., 1992. Tomographic imaging of P and S wave velocity structure beneath northeastern Japan. J. Geophys. Res. Solid Earth 97 (B13), 19909–19928. https://doi.org/10.1029/92JB00603.
Zhao, H., 2004. A fast sweeping method for eikonal equations. Math. Comput. 74, 603–627.
Zhou, X., Lan, H., Chen, L., Guo, G., 2020. The factored eikonal equation in curvilinear coordinate system and its numerical solution. Chin. J. Geophys. 63 (2), 638–651. https://doi.org/10.6038/cjg2020N0185 (in Chinese).